Progress In Electromagnetics Research C, Vol. 107, 33–47, 2021

Predictive Capacity of FDTD Method Embedding MTLN Technique for Lightning and HIRF Threats

Guadalupe G. Gutierrez[1, *], Tim McDonald[2], Carlos R. Paños[1], Raul Molero[3], Hugo Tavares[4], Hirahi Galindo[1], and Enrique Pascual-Gil[1]

Abstract—In this paper, the effectiveness for inferring the responses to electromagnetic threats of the finite difference time domain method combined with a multi-conductor, multi-shield, and multi-branched cable harness transmission line solver is validated by comparing simulation results with measurements performed on an equipped cockpit partially made by carbon fiber composite. A complete lightning indirect effects and high-intensity radiated field testing campaign was carried out in this cockpit within the scope of the European research and technology project Clean Sky 2 whose main goal is to reduce the aviation environmental impact by, for instance, building low-weight aircrafts with the increasing use of carbon fiber. Simulations are performed with EMA3D and MHARNESS obtaining very good agreement with measurements for a variety of observables and in a wide frequency range, thus proving the predictive capacity of these numerical methods for estimating the electromagnetic behavior of complex structures.

1. INTRODUCTION

The current trend in the use of electromagnetic (EM) simulations in the field of aeronautics since the earlier stages of proof of concept and design until the certification and even the maintainability of an aircraft makes necessary the development of numerical methods and their implementation in versatile and accurate tools which permit to solve the whole variety of configurations whose EM behavior need to be predicted [1–6].

CaPAbilities for innovative Structural and functional teSting of AeROstructures (PASSARO) [7] is a European Research and Technology project defined within the scope of Clean Sky 2 [8] focused on the design of the A/C of the future: an ultra-green and highly cost-efficient air-transport system. Its objective is to speed up technological breakthrough developments and to shorten the time-to-market for new solutions that introduce green technology into aviation.

In the work package titled 'EM compatibility environment assessment of panels structures and full scale demonstrator', the main electromagnetic compatibility (EMC) external threats that an aircraft can be subjected to are studied. To this end, a complete lightning indirect effect (LIE) and high-intensity radiated field (HIRF) testing campaign was carried out at Airbus Defence and Space (ADS) [9] EMC testing facilities on an aircraft cockpit manufactured as an hybrid structure composed of metal, carbon fiber composite (CFC), and CFC plus expanded cooper foil (ECF). This cockpit was equipped with a realistic electrical installation including 7 metal boxes as dummy equipment and 2 over-braided harnesses with several inner conductors.

The complete LIE and HIRF testing campaign comprises three measurement techniques: Low Level Direct Drive (LLDD), Low Level Swept Current (LLSC) and Low Level Swept Fields (LLSF). These

Received 20 September 2020, Accepted 16 November 2020, Scheduled 25 November 2020

* Corresponding author: Guadalupe G. Gutierrez (Guadalupe.Gutierrez@airbus.com).

[1] Computational Electromagnetics area within EME and Antenna Systems Engineering Department at Airbus Defence and Space, Getafe, Spain. [2] EMA, Inc. in Denver, Colorado, USA. [3] EMC Testing Department at Airbus Defence and Space, Getafe, Spain. [4] Electro-Magnetic Environmental Effects Department at Instituto de Soldadura e Qualidade, Oeiras, Portugal.

Figure 1. Test Case. DCI set-up with cage return (top-left), LLSF set-up with BiConiLog antenna and Double Ridge Waveguide Horn at 10 m distance from the cockpit (top-right), and LLSC set-up with 14.5 m long horizontal dipole and BiConiLog antenna at 20 m distance from cockpit (bottom).

three test set-ups can be seen in Fig. 1. LLDD consists of a low level Direct Current Injection (DCI) [10–13] whose objective is to relate the currents induced into the cables due to an applied external field by relating, in a first step, these currents with the surface current densities excited in the aircraft skin by measurements, and, in a second step, the surface current densities excited in the aircraft skin with the applied external field by simulations. This technique is needed from 10 kHz up to 2 MHz due to the difficulty of having a good radiating antenna at this lower frequency range, and its results are normally used up to the first resonant frequency of the object. In order to reduce the error when extrapolating the measured results to in-flight conditions, it is recommended the use of a cage return wire network arranged around the object under test [10, 11], so as to improve the homogeneity in the surface current distribution and reduce the reflection coefficient. This measurement technique is used to demonstrate compliance with lightning regulation [11] and also in the lower frequency range of HIRF [10]. During LLSC [10], applied from 2 to 400 MHz, the test object is situated on a metallic ground plane and it is illuminated by a low level EM field from different directions and polarizations, and the induced currents in the cables connecting the equipment are measured being able to determine a transfer function between the illuminating EM fields and the induced currents. From 100 MHz up to 18 GHz, LLSF technique is applied [10], which relates the internal HIRF environment at the location of the relevant electric or electronic systems with the external HIRF threat.

An EM model of this cockpit was generated by ADS using CATIA software [14]. It was the input for a finite difference time domain (FDTD) solver called EMA3D [15] embedding a multi-conductor transmission line network (MTLN) solver called MHARNESS. By means of simulations, surface current densities, current induced on over-braids, currents coupled on inner conductors and electric field (E) levels inside the cavity have been calculated in the different frequency ranges applicable and compared with the measurements.

This kind of validations shows the potential of EM simulations to estimate the transients induced in the aircraft from the beginning of its design, during the whole qualification and certification process, up to its maintenance, thus improving the safety and saving costs. The scarce literature published on this subject is detailed in following sections. The present study is more complete than those published before because it validates the simulations against measurements in a wide frequency range in which three different measurement techniques have to be used. In addition, due to the fact that the test case is a complex and hybrid metal-composite structure. And finally, because the present validation includes observables from currents on the object skin, passing through the field entering into the cavities and

the currents induced on the harnesses, down to the currents coupled to equipment individual pins.

The rest of the paper is organized as follows. Firstly, a description of the EM model and the tools used to perform the simulations are presented. Secondly, the pass/fail criterion used to draw conclusions is explained, and the obtained results are analyzed and compared to the measured values. Finally, most important conclusions are summarized.

2. MODEL DESCRIPTION

An EM model was generated by ADS, from the digital mock-up of the cockpit in CATIA. The model consists of a full scale cockpit demonstrator approximately 4 m long, 2.9 m wide and 2.6 m high, and has a hybrid construction based on the integration of CFC and metallic components (Fig. 2).

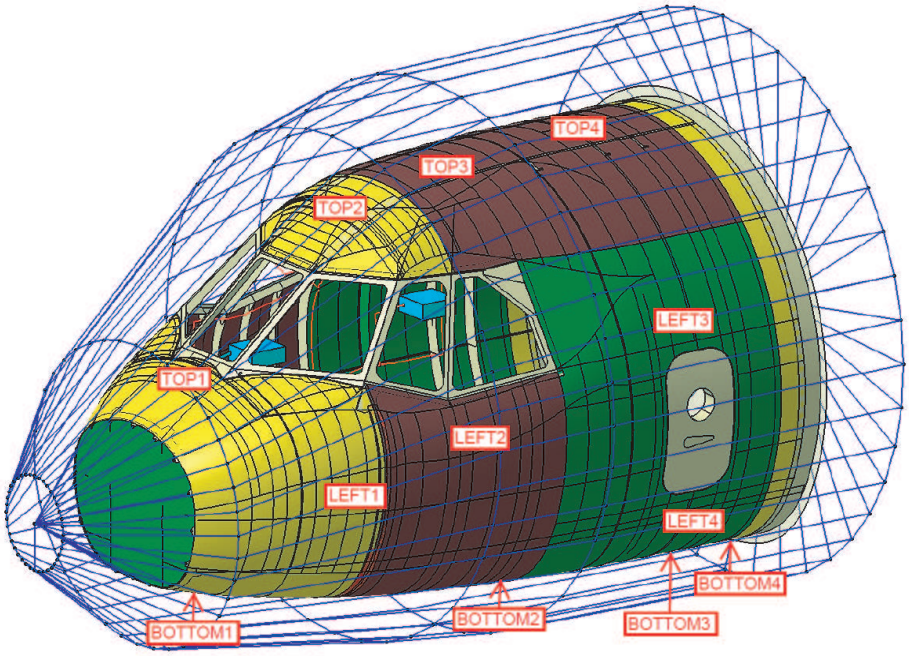

Figure 2. 3D EM model (Perfect Electric Conductor (PEC) materials are in yellow, CFC in green, CFC+ECF in brown, emergency door and internal structure modeled as PEC are in beige, equipment in cyan, harnesses in red, and cage return wire network in blue). Probe locations for surface current density are tagged (there are other four points at the right-hand side approximately symmetric to the ones on the left-hand side).

An extremely simplified EM model was used to perform the simulations, so that it is light, manageable and simple, and, at the same time, assures the necessary contacts between pieces and avoids the unwanted connections [16–19].

The cockpit is equipped with an electrical installation representative of an aircraft one with two over-braided harnesses. One of them is mainly routed on the top half of the cockpit and other one is mainly routed on the bottom volume below the cockpit floor, as can be seen in Fig. 3 (cockpit floor has not been included in the model because it is non-conductive). Each harness has several branches ended at metal boxes as items of equipment, making a total of 7 boxes grounded to the structure. The harnesses are filled with several inner conductors either with 50 Ω, short circuit or open circuit at their terminations, so as to analyze different configurations covering the whole range of impedance values. Depending on the number of inner conductors and the cable routing, two over-braid sizes are used.

In the frequency range of the DCI method, we modeled the complete test set-up, including the cage return wire network, the injection rig and the exit rig (see Fig. 2). The model was excited with a Gaussian pulse covering the frequency range of interest, applied as a voltage source in the injection line.

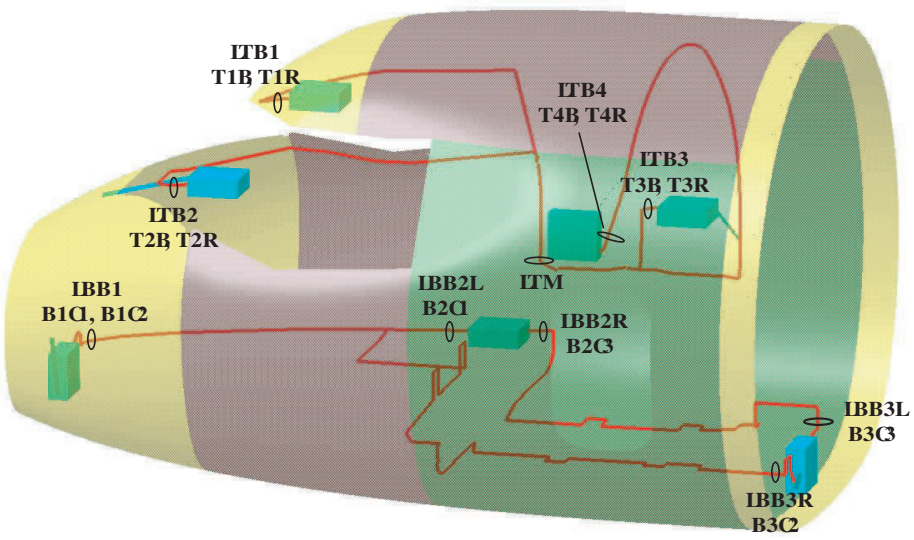

Figure 3. Top Harness and Bottom Harness routes. Probe locations for currents induced on over-braids and inner conductors are tagged.

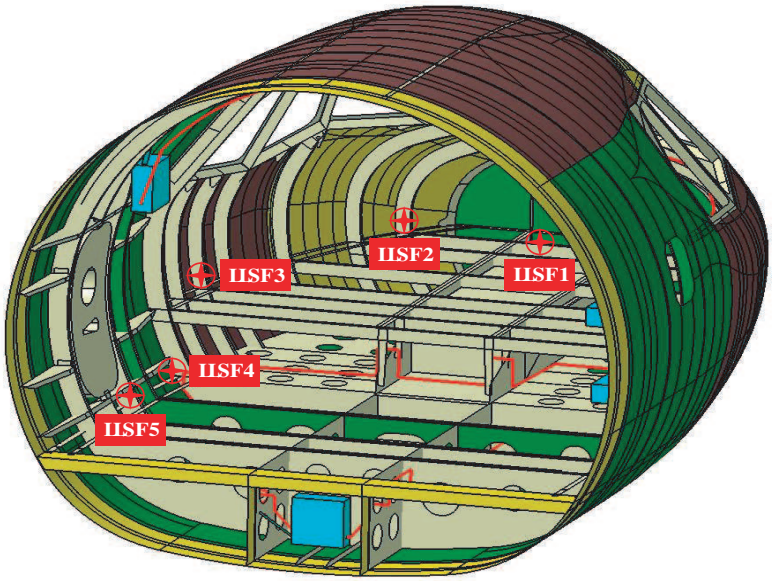

Figure 4. Probe locations for electric field.

Whereas, for LLSC and LLSF, a plane-wave (PW) was used as illumination source, considering in this way 'in-flight' conditions. Also, Gaussian pulses covering in each case the frequency range of interest were used, being, in these cases, the incident electric field. Radiating antennas and metallic ground plane embedded in the concrete floor of the Open Area Test Site (OATS) where testing campaign took place were not included in the EM model for the sake of a reduction in the computational cost and because they have little influence for most of the frequencies [20, 21].

Both in measurements and in simulations, for conductive effects, current probes at every over-braid branch and every inner conductor are monitored, while, for radiated effects, electric field probes are placed at different locations inside the main cavity of the cockpit, positioned below the different materials present in the cockpit (metal, CFC, and CFC with ECF). In addition, surface current density probes are located at several positions, also made of different materials, over the aerodynamic surface of the cockpit as required in the DCI test. In Figs. 2, 3, and 4 the analyzed probe locations are tagged.

3. SIMULATION TOOLS, PARAMETERS AND POST-PROCESS.

EMA3D is a commercial implementation of the FDTD method of solving Maxwell's equations [22] using the staggered-grid technique introduced by Yee in [23]. EMA3D implements surface and line representations in addition to volume elements. Furthermore, EMA3D includes sub-cell modeling features such as a composite material algorithm that resolves surfaces smaller than the computational cell size, including skin depth effects.

Another important modification is that three-dimensional (3D) lines may be modeled to include an integrated, hybridized MTLN solver called MHARNESS. The MTLN solver is an FDTD solution of the Telegrapher's equations in one-dimension (1D) [24]. The inductance and capacitance matrices are simulated in two-dimensions (2D) using an electrostatic solver for the cross-section for each cable segment's arrangement of conductors and shields. Once the matrix calculation is computed, the 1D FDTD solver proceeds down each line to complete the electromagnetic response.

Traditional transmission line theory is modified by the inclusion of multiple topological levels or shields. The levels are connected to one another through the shield transfer impedance, an intrinsic measure of the ratio of voltage on an inner pin and the current outside a shield [25]. Further, the MTLN solver is integrated as a line in the 3D FDTD solver. There is two-way communication and flow of energy between the MTLN solver and the 3D solver, implemented through the electric field in both step equations. In other words, as the simulations steps forward in time, both the 3D FDTD and the 1D MTLN solver perform a self-consistent calculation of the fields in the presence of each other before each advancing to the next time-step [26].

As the MTLN wire radius becomes comparable to the 3D cell size, traditional hybrid methods require the use of additional cell locations on the sides of each wire to resolve the integrated MTLN and 3D FDTD electric field. The result of this extra buffer on the sides of the wire can be problematic to route a large number of harnesses in a small area. The traditional FDTD wire model [27] is adjusted by a "packing factor" which tracks the buffer electric fields separately from the space around the wire and allows for integrated MTLN harness model diameters comparable to the cell size, thus allowing for more realistic spacing of cables within the volume.

As a result, the integrated cable harness solver and 3D FDTD solver allow the modeling of large aircrafts, with dimensions of many meters, while resolving conductor pins, which are of milimeter or even sub-millimeter dimensions. This hybrid technique combined with domain decomposition parallelization using Message Passing Interface (MPI) [28] allows for computationally-efficient modeling of full aircraft down to individual pins. This hybrid technique has been previously validated on full aircraft compared to simulation [29].

A Cartesian FDTD mesh with a constant space-step of 10 mm was employed for the simulations [15, 30]. Perfect matching layer (PML) with eight cells absorbing boundary conditions were employed to truncate the domain, yielding a problem size of almost 100 Mcells. A time-step of 9 ps was employed to meet the Courant-Friedrichs-Lewy (CFL) stability condition [31]. For conductive effects (DCI and LLSC), a total time of 60 µs was simulated, which was sufficient to obtain reasonable convergence of the currents, and 30 µs to get convergence of the H fields or surface current densities. For radiated effects (LLSF), running during 30 µs is enough to get convergence.

A computation speed of around 5 Mcells per second and core was reached in an Intel Xeon Gold 6154 cluster with 18 cores per processor and 2 processors per node of 3.00 GHz frequency and 192 GB RAM memory each node, dividing the problem volume into as many blocks as desired MPI processes according to the number of available cores.

Over-braids are simulated with almost their real radii, being 3.75 or 4.48 mm depending on the branch, and with a packing factor between 80 and 90%. They have assigned a resistance per unit length of 4.59 or 3.57 mΩ/m respectively, according to the over-braid data-sheets. During the testing campaign, the bonding between each over-braid branch and their corresponding shielded box was measured in order to check the good connection of the harnesses. Those values were used to assign a connection resistance to each over-braid end. Inner conductor radius is around 0.28 mm and a jacket with a relative permittivity value of 2.1 is over every one of them. A resistance per unit length of 77.6 mΩ/m is assigned to them, as specified in the wire data-sheet. They are ended on 50 Ω, short circuit or open circuit according to their real configuration in the cockpit demonstrator.

In the post-process, simulation outcomes are interpolated to the same number of frequency points

measured during the testing campaign, which consist of 801 linearly spaced points per decade in DCI frequency range, around 600 linearly spaced points in LLSC frequency range, and 1000 logarithmically spaced points in LLSF frequency range. After that, a 5% averaging bandwidth filter is also applied, in linear values, to every simulated and measured curve in order to clean them and make easier the comparisons. It is centered at the frequency of interest with an averaging bandwidth of 2.5% on each side, leading to an acceptable curve smoothing [10].

Finally, the filtered simulated responses have been post-processed to calculate the envelopes used to obtain the masks needed for determining the system test levels [10]. Thus, for currents induced on cables in DCI and LLSC, an octave envelope has been generated by extending the value of each resonant peak down to one half and up to two times the frequency of the peaks. For LLSF attenuation values, a 10% sliding frequency window envelope has been generated by using maximum amplitude of the curve within a sliding frequency window that is ±10 percent of any given frequency.

4. PASS/FAIL CRITERION

There are different approaches which can help us to assess the agreement between two curves, such as the analysis of an expert eye, the Feature Selective Validation (FSV) method [32], or the HIRF-SE project approach [1] based on the post-process established in [10]. In this paper, a methodology focused on expert eye, but which uses some objective data also based on the post-process defined in [10] is established in order to define a pass/fail criterion to assess the comparison between measurements and simulations.

For safety and certification purposes, one important issue is the fact that, wherever there is not a perfect matching between simulations and measurements, the simulated values are conservative. In our model, this conservativeness of simulated results can come from the lack of some cable features on cabling definition, such as skin depth or variations in inner conductor locations, and the lack of some absorbers which were present in the real cockpit mainly to support the cockpit itself, equipment and probes. In the cases of DCI and LLSC, where the observables are the induced currents normalized by the injected current or the incident field respectively, being conservative is that simulations overestimate the measurements, since the higher coupling on wiring, the worse for EM protection. However, for LLSF the observable is the attenuation, and, therefore, being conservative is to underestimate it, since the less the structure attenuates the incident field, the worse for EM protection.

For DCI frequency range, most important feature is the level of the first resonant peak which appears in the response, because highest induction level in the frequency range where DCI technique is applied, is usually found at the first resonance. In addition, the conservativeness of simulated results is analyzed putting the focus on the deviation where simulation envelopes do not cover measurements. Consequently, Table 2 shows the probe names in the first column, the difference in dB between the first resonant peak value of the simulated and the measured curves in the second column, and, in the following columns, the percentage of spot frequencies for which the difference between the octave envelope for the simulated values and the measured values is higher than 0 dB, −6 dB, or −10 dB, respectively. Then, a color code was applied to assess the obtained results. For the level difference (second column), dark green stands for the deviations lower than ±6 dB, yellow stands for deviations between ±6 dB and ±10 dB, and red stands for deviations higher than ±10 dB. For percentages columns (third, fourth and fifth), dark green is used for values between 90 and 100% of points overestimated what is considered a very good agreement, light green for values between 75 and 90% of points overestimated what is considered a good agreement, yellow for values between 50 and 75% of points overestimated what is considered a fair agreement, and red for values under 50% of point overestimated what is considered a poor agreement.

For LLSC, in view of the measured curves, the most important feature has been selected at the higher resonant level in the range between 100 and 160 MHz, where higher resonances are found due to the object dimensions. Measurements up to 10 MHz have been discarded because the antenna efficiency at these low frequencies was not good and the obtained measurements are not correct. Therefore, Table 3 is created similarly to Table 2, showing in the second column the difference between the level of the octave envelopes for the simulated and the measured data for the mentioned frequency range.

For LLSF, the most important feature is the mean attenuation level provided by the structure,

which is higher at the low frequency range and lower at the high frequency range [33], and the relevant peaks at some risky frequencies, if any. Consequently, Table 4 shows the probe names in the first column, the difference in dB between the measured and the simulated mean attenuation levels in the range between 100 and 400 MHz in the second column (labeled as Low Frequency (LF) in Table 4), the difference in dB between the measured and the simulated mean attenuation levels in the range between 400 MHz and 3 GHz in the third column (labeled as High Frequency (HF) in Table 4), and, in the following columns, the percentage of spot frequencies for which the 10% sliding frequency window envelope for the simulated values underestimates the measured values in less than or equal to 0 dB, −6 dB or −10 dB, respectively. Then, a color code analogous to the one mentioned above was applied to this table.

Table 1 summarises the pass/fail criterion selected, according to each kind of test, which has been explained in the previous paragraphs.

Table 1. Pass/fail criterion summary.

<table>
<tr><th colspan="2">Pass/Fail Criterion</th><th>DCI</th><th>LLSC</th><th>LLSF</th></tr>
<tr><td rowspan="5">Main features</td><td rowspan="3">Definition</td><td rowspan="3">amplitude level in dB of the 1st resonant peak</td><td rowspan="3">higher resonant amplitude level in dB in the frequency range with higher induction level</td><td>mean attenuation level in dB provided by the structure 100 MHz - 400 MHz</td></tr>
<tr><td>mean attenuation level in dB provided by the structure 400MHz - 3 GHz</td></tr>
<tr><td>relevant peaks at some risky frequencies, if any</td></tr>
<tr><td rowspan="3">Color code</td><td colspan="3">dark green → deviation ≤ ±6 dB</td></tr>
<tr><td colspan="3">yellow → ±6 dB ≤ deviation ≤ ± 10 dB</td></tr>
<tr><td colspan="3">red → ±10dB ≤ deviation</td></tr>
<tr><td rowspan="5">Conservative values</td><td>Definition</td><td>overestimate induced currents</td><td>overestimate induced currents</td><td>underestimate attenuation</td></tr>
<tr><td rowspan="4">Color code</td><td colspan="3">dark green → 100% ≤ conservative frequency spots ≤ 90%</td></tr>
<tr><td colspan="3">light green → 90% ≤ conservative frequency spots ≤ 75%</td></tr>
<tr><td colspan="3">yellow → 75% ≤ conservative frequency spots ≤ 50%</td></tr>
<tr><td colspan="3">red → 50% ≤ conservative frequency spots ≤ 0%</td></tr>
</table>

5. RESULT ANALYSIS

5.1. DCI

For DCI, the agreement in the longitudinal current densities, currents induced on over-braids and currents coupled on inner conductors is very good. Fig. 5 shows the comparison for surface current density probes located at top/bottom/left/right cockpit skin points over metal/CFC/CFC+ECF material as some examples. Regarding the wiring, Table 2 summarizes the results obtained for the selected features. The 10 first rows, whose probe name starts by the letter L, corresponds to probes on over-braids, whereas the 14 last rows corresponds to probes on inner conductors (probes whose name starts by T concern top harness, while probes whose name starts by B concern bottom harness). For inner conductors belonging to top harness, the ones whose probe name ends by the letter R are ended in 50 Ω (R because red colored cables were used for those routes), and the ones whose probe name ends by the letter B are ended in short circuit (B because blue colored cables were used for those routes); the rest of branches are ended in open circuit and have not been shown in the result tables because the

Table 2. DCI result assessment.

Probe	Level Diff (dB)	0 dB (%)	−6 dB (%)	−10 dB (%)
LTB1	1.62	24	54	100
LTB2	−1.76	71	96	100
LTB3	3.86	23	74	100
LTB4	0.84	31	34	36
LTM	1.81	24	73	100
LBB1	5.55	100	100	100
LBB2L	10.81	88	100	100
LBB2R	7.90	37	82	100
LBB3L	2.81	25	100	100
LBB3R	10.73	26	92	96
T1B	11.21	95	98	100
T1R	13.63	93	96	98
T2B	18.33	100	100	100
T2R	18.08	63	80	88
T3B	17.81	72	94	100
T3R	11.90	94	97	98
T4B	4.06	66	78	83
T4R	12.15	76	90	95
B1C1	6.33	25	25	31
B1C2	1.33	41	65	71
B2C1	5.86	35	48	55
B2C3	13.09	92	96	98
B3C2	1.70	56	93	98
B3C3	12.42	96	99	100

currents induced on them are near zero. Whereas, inner conductors belonging to bottom harness are all ended in short circuit.

Figures 6 and 7 show the comparison between simulated and measured curves, along with the octave envelope of simulated data, for some of the over-braid and the inner conductor probes respectively. One of the worse results obtained in Table 2 for the over-braids is the LBB3R, and, even for this case, the agreement is probably not poor for an expert opinion. Another questionable result is found for LTB4 due to the few overestimated points, and, again, even for this case, the curves are near for the higher induced currents. For inner conductors, worse results are found for T2B and B1C1, but the curve comparisons show many similarities. We can conclude that results obtained for DCI are good in general, with a mean first resonance deviation (arithmetic mean of the values in the second column of Table 2) of 4.77 dB for over-braids and 10.56 dB for inner conductors. The deviations obtained can be due to inaccuracies, uncertainties or errors in the simulation or in the measurement processes. In particular, non conservative values mainly come from low frequency results, where simulations are affected by the convergence of the responses; however, induced levels at these frequencies are low and, therefore, not a concern for aircraft protection.

As shown before, the agreement obtained for DCI is very good for superficial currents and good for currents induced on the wiring. It is acceptable even for currents induced on inner conductors, which could permit the use of predicted values for determining levels for the pin injection test employed in lightning certification [33]. Likewise, good results for DCI validation have also been achieved mainly for surface current density and even for currents induced along over-braids in previous works as [34–39], but with no validation of currents induced on inner conductors.

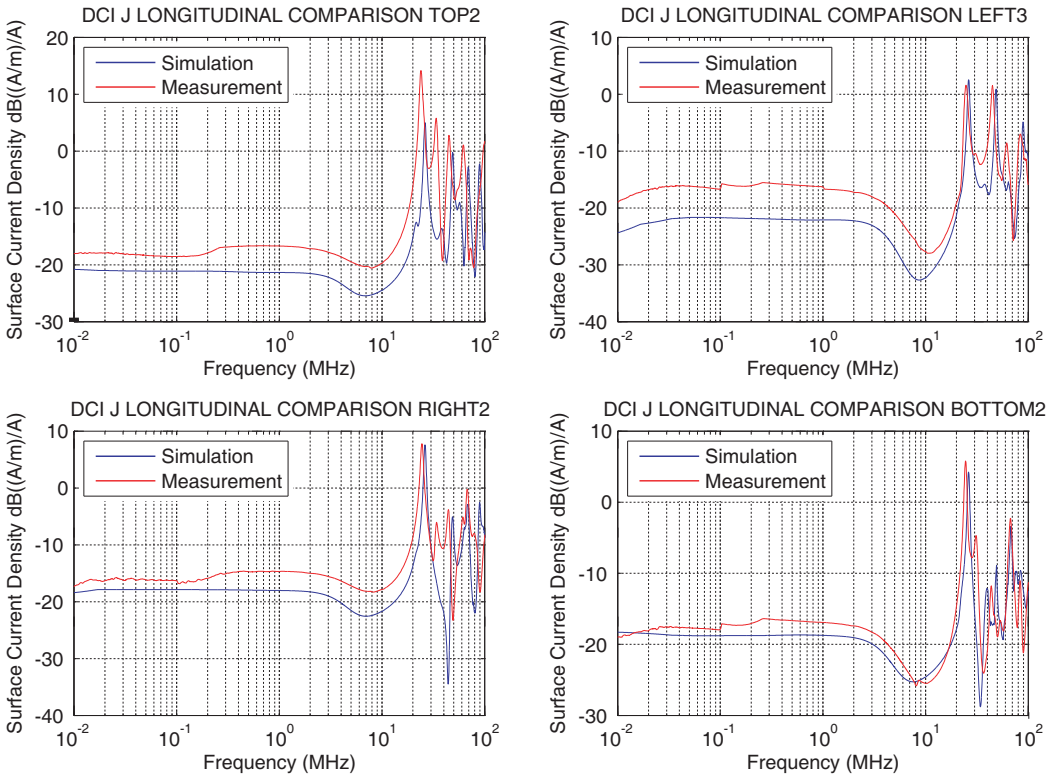

Figure 5. DCI — Surface current densities (see probe locations in Fig. 2).

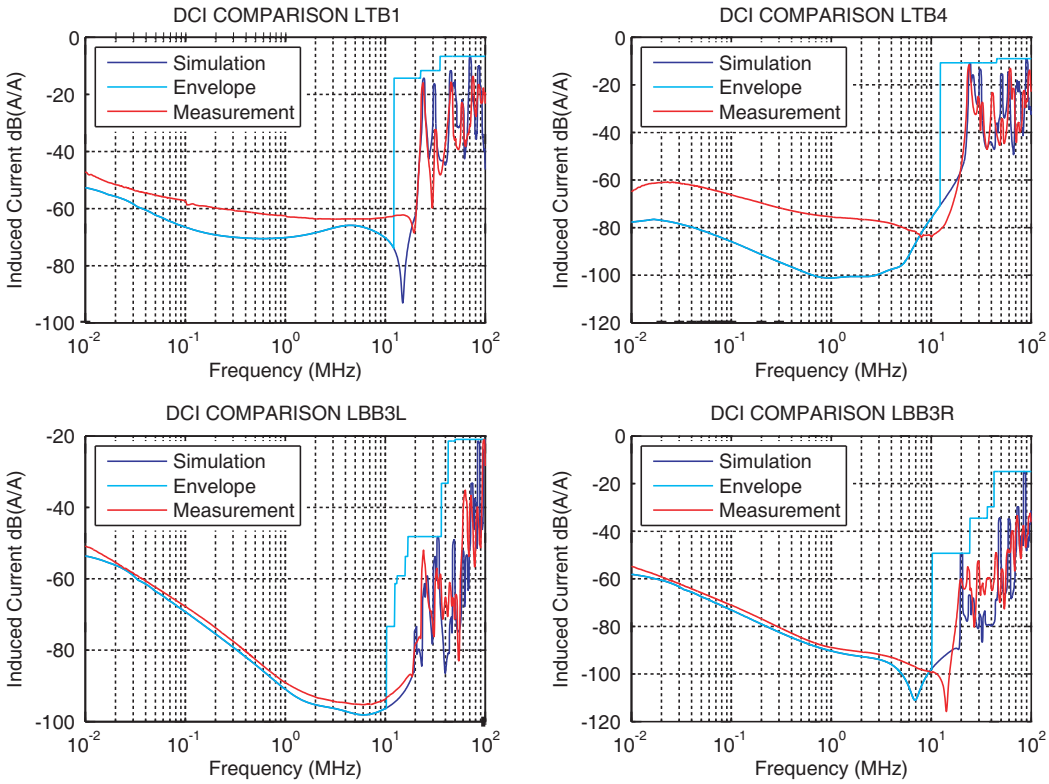

Figure 6. DCI — Currents induced on over-braids (see probe locations in Fig. 3).

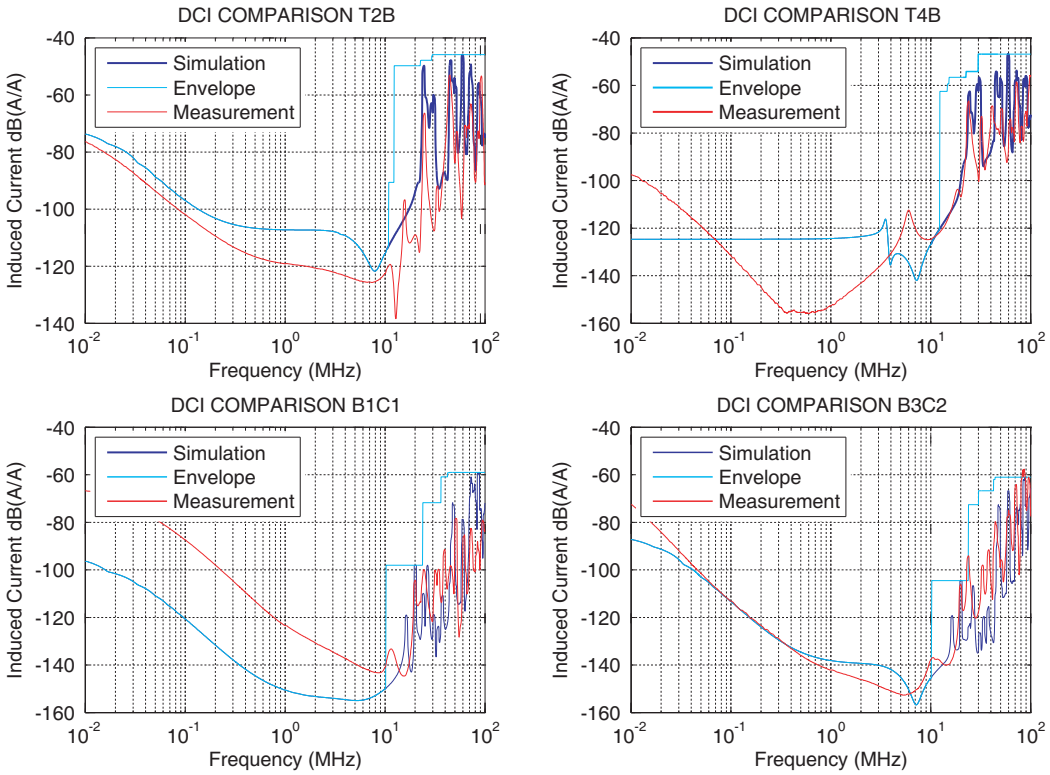

Figure 7. DCI — Currents induced on inner conductors (see probe locations in Fig. 3).

5.2. LLSC

Illumination angle at 45 degrees in the azimuth plane and horizontal polarization has been used to perform the present validation. Table 3 summarizes the results obtained for the selected features. For over-braids, the mean difference in level (arithmetic mean of the values in the second column of Table 3) is 7 dB, while, for inner conductors, it is of 13.35 dB. Even though these results are not very good, simulated results are conservative for the majority of the cases, especially for inner conductors, which are good news for safety and certification points of view. It is known that LLSC simulations will over-predict compared to measurements without including simulation features such as skin depth and variations in inner conductor locations [24], so, in this sense, the analysis is intended to be conservative. Comparison graphs between simulated and measured curves, along with the octave envelope of the simulated data, for some of the over-braid and inner conductor probes can be seen in Fig. 8.

There are not many LLSC validations in previous works and even fewer for complex structures. In [21, 37, 39, 40] can be found some examples, but, again, with no validation of currents induced on inner conductors. The validation of a LLSC test is the most complex one since both simulations and measurements have more uncertainty in this frequency range. On the one hand, regarding simulations, the need of an accurate and complete model is greater in the intermediate frequency range than at the lower or higher ones, since model details both near and far from the probe locations can affect the results, both conducted and radiated effects are present and contributing together to the EM behavior, and also because, especially for the lower frequencies, the illuminating wave is not plane in the test set-up and, therefore, the in-flight approach should be replaced by the inclusion of antenna models in the simulations to compare their results with measured data. On the other hand, regarding measurements, as mentioned above, frequencies between 2 and 10 MHz were not correctly captured since the available power was not enough to generate moderate currents induced on bundles. Besides, the calibration process at the central point without the aircraft present involves a slight additional uncertainty.

Table 3. LLSC result assessment.

Probe	Level Diff (dB)	0 dB (%)	−6 dB (%)	−10 dB (%)
LTB1	−16.03	37	58	79
LTB2	−12.14	65	85	96
LTB3	−2.06	73	87	88
LTB4	−9.46	74	94	97
LTM	2.63	100	100	100
LBB1	−6.36	79	89	93
LBB2L	2.4	85	90	92
LBB2R	−3.86	77	87	89
LBB3L	0.97	76	87	87
LBB3R	−14.05	67	84	92
T1B	14.74	100	100	100
T1R	13.17	99	100	100
T2B	13.87	100	100	100
T2R	15.99	100	100	100
T3B	19.51	100	100	100
T3R	12.84	99	100	100
T4B	5.53	100	100	100
T4R	4.67	100	100	100
B1C1	24.03	98	99	100
B1C2	11.51	99	100	100
B2C1	13.58	99	100	100
B2C3	9.16	90	90	90
B3C2	16.88	100	100	100
B3C3	11.41	90	90	90

5.3. LLSF

Illumination angle of 0 degrees in the azimuth plane and horizontal polarization has been used to perform the present validation, and the obtained agreement is very good as shown in Table 4. The mean level difference is 3.22 dB for the low frequency range (arithmetic mean of the values in the second column of Table 4) and 3.30 dB for the high frequency range (arithmetic mean of the values in the third column of Table 4), and the attenuation value at the great majority of frequencies is underestimated,

Table 4. LLSF result assessment.

Probe Name	LF Level Diff (dB)	HF Level Diff (dB)	0 dB (%)	−6 dB (%)	−10 dB (%)
LLSF1	9.09	5.72	97	100	100
LLSF2	0.94	2.89	91	100	100
LLSF3	-0.84	2.96	85	99	100
LLSF4	2.41	2.88	92	100	100
LLSF5	2.84	2.06	87	98	99

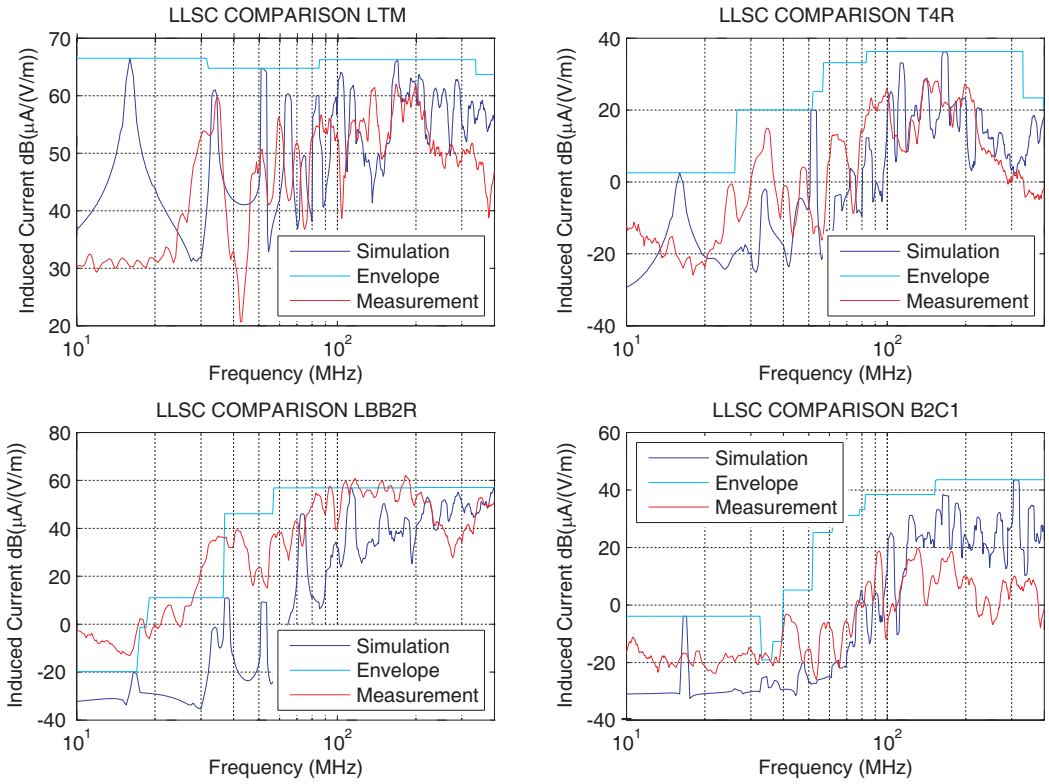

Figure 8. LLSC — Induced Currents (see probe locations in Fig. 3).

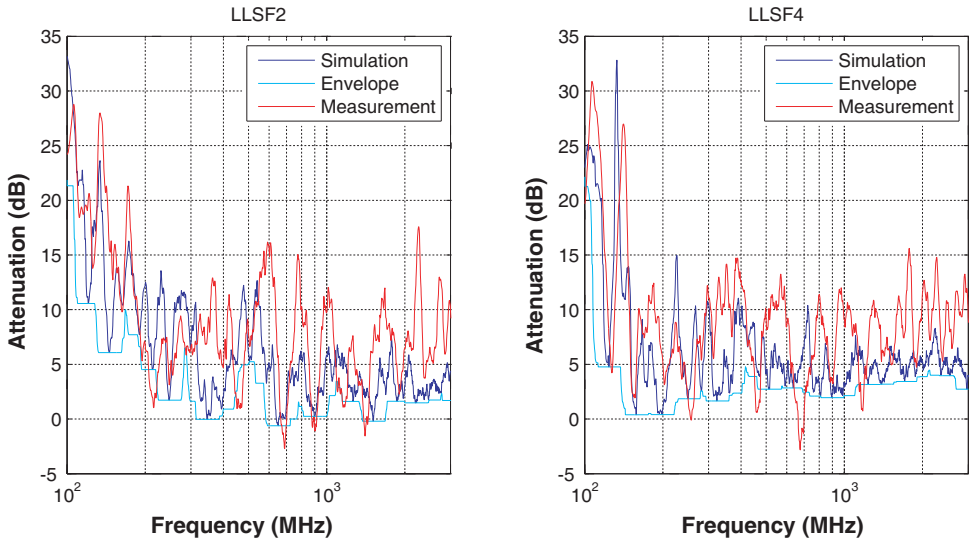

Figure 9. LLSF — Attenuation (see probe locations in Fig. 4).

in other words, the simulated results are conservative. Fig. 9 shows two examples of the comparison between simulated and measured curves, along with the 10% sliding frequency window envelope of the simulated data, for different locations in the cavity on the left side below metal and CFC, respectively.

Again, there is little literature regarding LLSF validations and even fewer for complex structures [37, 39, 41, 42]. However, the good results shown in most of them and also in the present study reveal the suitability of this kind of simulations for shielding effectiveness estimation.

6. CONCLUSIONS

EM models and numerical codes are useful and powerful tools which can predict the EM behavior and carry out parametrical studies during the design phase of an aircraft, when changes are simpler and less costly, with the potential benefit of improving aircraft safety. In the subsequent phases like certification or maintenance, time of aircraft testing can be saved performing analysis by EM simulations.

In the present paper, the validation of the simulations, performed with an FDTD method, EMA3D, combined with a MTLN solver, MHARNESS, compared with measurements carried out on an aeronautic complex structure with a controlled configuration of electrical installation, is presented for a wide frequency spectrum using the different testing techniques applicable for each frequency range.

The obtained agreement between measurements and simulations is good for lower and higher frequencies (below tens of MHz and above hundreds of MHz) and fair in the intermediate frequency range. It must be taken into account that we are considering observables as different as surface current density, current induced on over-braids, current coupled on inner conductors and electric field. Note that this study covers the main EMC external threats that an aircraft can be subjected to.

The obtained good agreement proves the effectiveness of these methods and their predictive capacity. Thus, a step forward is taken in order to use EM simulations in every stage from the design to the end of service of an aircraft.

ACKNOWLEDGMENT

The work described in this paper has received funding from the European Community's H2020-EU.3.4.5.4. — ITD Airframe Programme with Topic CS2-GAM-2018-AIR — Airframes under grant agreement ID 807083.

REFERENCES

1. HIRF-SE project European Commission, Dec. 2008–May 2013, http://www.hirf-se.eu.
2. UAVEMI, http://www.inta.es/opencms/export/sites/default/INTA/es/bolsa-deempleo/oportunidad_1489394499029.
3. UAVE3, http://www.inta.es/WEB/uave3/en/objectives.
4. Clean Sky, https://www.cleansky.eu.
5. EPICEA project European Commission Horizon 2020, Feb. 2016–Jan. 2019, http://epicea-env714.
6. EUROCAE WG31, http://www.eurocae.net/about-us/working-groups.
7. PASSARO, http://passaro.inegi.up.pt/index.asp.
8. Clean Sky 2, https://www.cleansky.eu/innovative-technologies-0.
9. Airbus Defence and Space, https://www.airbus.com/defence.html.
10. EUROCAE ED-107, rev A, Jul. 2010/SAE ARP 5583, "Guide to certification of aircraft in a high-intensity radiated field (HIRF) environment," rev A, Jun. 2010.
11. EUROCAE ED-105, rev A, Jul. 2013/SAE ARP 5416, "Aircraft lightning test methods," rev A, Jan. 2013.
12. Rothenhausler, M., A. Ruhfass, and T. Leibl, "Broadband DCI as a multi usable EMC-test method," *2008 IEEE International Symposium on Electromagnetic Compatibility*, 1–5, Aug. 2008.
13. Zhang, B. and U. Jiang, "Research progress of direct current injection technique in aircraft emc test," *2009 3rd IEEE International Symposium on Microwave, Antenna, Propagation and EMC Technologies for Wireless Communications*, 843–849, Oct. 2009.
14. CATIA by Dassault Systemes, http://www.3ds.com.
15. EMA3D, https://www.ema3d.com.
16. Gutiérrez, G. G., E. P. Gil, D. G. Gómez, and J. I. P. Gómez, "Finite-difference time-domain method applied to lightning simulation and aircraft certification process," *International Symposium on Electromagnetic Compatibility EMC Europe*, York, UK, 2011.

17. Gil, E. P. and G. G. Gutierrez, "Simplification and cleaning of complex CAD models for EMC simulations," *International Symposium on Electromagnetic Compatibility EMC Europe*, York, UK, 2011.
18. Gutierrez, G. G., S. F. Romero, M. Gonzaga, E. Pascual-Gil, L. D. Angulo, M. R. Cabello, and S. G. Garcia, "Influence of geometric simplifications on lightning strike simulations," *Progress In Electromagnetics Research C*, Vol. 83, 15–32, 2018.
19. Gutierrez, G. G., S. F. Romero, M. Gonzaga, E. Pascual-Gil, L. D. Angulo, M. R. Cabello, and S. G. Garcia, "Influence of geometric simplifications on high-intensity radiated field simulations," *Progress In Electromagnetics Research C*, Vol. 86, 217–232, 2018.
20. Fernández Romero, S., P. López Rodríguez, D. Escot Bocanegra, D. Poyatos Martínez, and M. Añón Cancela, "Comparing open area test site and resonant chamber for unmanned aerial vehicle's highintensity radiated field testing," *IEEE Transactions on Electromagnetic Compatibility*, Vol. 60, No. 6, 1704–1711, 2018.
21. Gutierrez, G. G., S. F. Romero, J. Alvarez, S. G. Garcia, and E. P. Gil, "On the use of FDTD for HIRF validation and certification," *Progress In Electromagnetics Research Letters*, Vol. 32, 145–156, 2012.
22. Perala, R., T. Rudolph, P. McKenna, and C. Jones, "Application of numerical analysis to the electromagnetic effects validation of aircraft," *Proceedings AIAA/IEEE Digital Avionics Systems Conference*, IEEE, 1993.
23. Yee, K., "Numerical solution of initial boundary value problems involving maxwell's equations in isotropic media," *IEEE Transactions on Antennas and Propagation*, Vol. 14, No. 3, 302–307, 1966.
24. Weber, C., J. Kitaygorsky, G. Rigden, R. A. Perala, and R. Fisher, "Evaluation of complexity of wire harness models in a HIRF environment," *2013 IEEE International Symposium on Electromagnetic Compatibility*, IEEE, Aug. 2013.
25. Vanlandschoot, B. and L. Martens, "New method for measuring transfer impedance and transfer admittance of shields using a triaxial cell," *IEEE Transactions on Electromagnetic Compatibility*, Vol. 39, 180–185, May 1997.
26. Rigden, G. J., "Integration of multiconductor cable codes with three dimensional time domain finite difference electromagnetic solvers," *SAE Technical Paper, SAE International*, Sep. 2001.
27. Perala, R. A., G. J. Rigden, and J. R. Elliott, "A historical perspective of system-level TDFD EME simulation," *2007 IEEE International Symposium on Electromagnetic Compatibility*, 1–4, 2007.
28. McDonald, T., R. Fisher, G. Rigden, and R. Perala, "Parallel FDTD electromagnetic effects simulation using on-demand cloud HPC resources," *2013 IEEE International Symposium on Electromagnetic Compatibility*, IEEE, Aug. 2013.
29. Weber, C., J. A. de Souza Mariano, R. C. C. Freire, and E. Durso-Sabina, "Validation of numerical simulation approach for lightning transient analysis of a transport category aircraft," *2019 International Conference on Lightning and Static Electricity, ICOLSE*, 2019.
30. CADfix, http://www.transcendata.com/products/cadfix.
31. Taflove, A. and S. C. Hagness, *Computational Electrodynamics: The Finite-difference Time-domain Method*, 3rd Edition, Artech House, Boston, 2005.
32. IEEE Standard P1557, "Standard for validation of computational electromagnetics computer modelling and simulation," Part 1, 2, 2008.
33. RTCA/DO-160, issue G, Dec. 2010/EUROCAE ED-14, "Environmental conditions and test procedures for airborne equipment," issue G, May 2011.
34. Gil, E. P., G. G. Gutierrez, and R. M. Castejóon, "Application of advanced simulations in time domain in the EMC certification process of an aircraft," *Proceedings XXXIII URSI Symposium*, Granada, Spain, 2018.
35. Bastard, C., M. Meyer, C. Guiffaut, and A. Reineix, "Ways of improvement for HIRF transfer function assessment on rotorcraft," *2019 ESA Workshop on Aerospace EMC*, 1–6, May 2019.
36. Pérez, F. C., G. Gutierrez Gutierrez, H. Tavares, A. Khamlichi, J. M. Alberquilla, R. Molero Castejón, N. Matos, and A. R. Linares, "Lightning low level vs high level direct current

injection tests on a full scale aircraft cockpit," *2019 International Symposium on Electromagnetic Compatibility — EMC EUROPE*, 644–649, Sep. 2019.

37. Rasek, G. A., E. Pascual-Gil, A. Schröder, I. Junqua, R. Guidi, C. A. Kreller, H. Brüns, and S. E. Loos, "HIRF transfer functions of a fuselage model: Measurements and simulations," *IEEE Transactions on Electromagnetic Compatibility*, Vol. 56, 311–319, Apr. 2014.
38. Cabello, M. R., S. Fernández, M. Pous, E. Pascual-Gil, L. D. Angulo, P. López, P. J. Riu, G. G. Gutierrez, D. Mateos, D. Poyatos, M. Fernandez, J. Alvarez, M. F. Pantoja, M. Añón, F. Silva, A. R. Bretones, R. Trallero, L. Nu no, D. Escot, R. G. Martin, and S. G. Garcia, "SIVA UAV: A case study for the EMC analysis of composite air vehicles," *IEEE Transactions on Electromagnetic Compatibility*, Vol. 59, 1103–1113, Aug. 2017.
39. Rasek, G. A., A. Schröder, P. Tobola, Z. Řezníček, S. E. Loos, T. Tischler, and H. Brüns, "HIRF transfer function observations: Notes on results versus requirements and certification approach," *IEEE Transactions on Electromagnetic Compatibility*, Vol. 57, No. 2, 195–202, 2015.
40. Schickele, P., X. Ferrieres, and J. Parmantier, "FEM-MTLN hybridization technique to evaluate electrical current on multiconductor cables inside enclosures illuminated by a plane wave," *2019 International Applied Computational Electromagnetics Society Symposium (ACES)*, 1–2, Apr. 2019.
41. Gutierrez, G. G., J. Alvarez, E. Pascual-Gil, M. Bandinelli, R. Guidi, V. Martorelli, M. F. Pantoja, M. R. Cabello, and S. G. Garcia, "HIRF virtual testing on the C-295 aircraft: on the application of a pass/fail criterion and the FSV method," *IEEE Transactions on Electromagnetic Compatibility*, Vol. 56, No. 4, 854–863, 2014.
42. Romero, S. F., G. G. Gutierrez, A. L. Morales, and M. A. Cancela, "Validation procedure of low level coupling tests on real aircraft structure," *International Symposium on Electromagnetic Compatibility EMC*, Europe, 2012.